Available online at www.sciencedirect.com
ScienceDirect
Ceramics International 37 (2011) 3139–3152
CERAMICS INTERNATIONAL
www.elsevier.com/locate/ceramint

Synthesis of $CeAlO_3/CeO_2$–Al_2O_3 for use as a solid oxide fuel cell functional anode material

Selma A. Venâncio *, Paulo Emílio V. de Miranda

Hydrogen Laboratory, Coppe – Department of Metallurgy and Materials Engineering, Federal University of Rio de Janeiro, P.O. Box 68505-21942-972 Rio de Janeiro, RJ, Brazil

Received 15 February 2011; received in revised form 12 May 2011; accepted 16 May 2011
Available online 23 May 2011

Abstract

A composite electrocatalyst was developed to be fitted for the purpose of satisfying the features required for use as a solid oxide fuel cell functional anode material. The main functionality searched for was the ability to make the direct oxidation of carbon containing fuels in an SOFC without being severely coked. The present paper deals with the synthesis and characterization of such material. Therefore, ceramic electrocatalysts composed of $CeAlO_3$, CeO_2 and Al_2O_3 were synthesized by the amorphous citrate method and calcined at temperatures ranging from 300 °C to 900 °C. The synthesis procedures were designed to produce nanometric sized powders for which the calcination conditions were selected in order to fulfill requirements such as ease to be sintered; formation of selected phases upon calcinations at different temperatures; particle size control; surface area and morphology well suited for the production of ceramic suspensions to be processed into an SOFC functional anode. The main results have shown that increasing the calcination temperature under an oxidizing atmosphere induces the $CeAlO_3$ phase with a tetragonal perovskite type structure to undergo a phase transformation to CeO_2 (and Al_2O_3) with cubic fluorite type structure. However, the structure is able to be reversed and reduced back to the $CeAlO_3$ phase if calcined under a hydrogen atmosphere. The increase in the calcination temperature increases the particle average size, reduces the surface area and increases the material density, considering the same phase and crystalline structure. It was shown that the synthesis and calcinations procedures hinder the crystallographic identification of the presence of alumina.

Keywords: Cerium aluminate synthesis; Functional SOFC anode; Ceramic eletrocatalyst

1. Introduction

When the fuel option for a solid oxide fuel cell (SOFC) is a carbon containing fuel to be used without pre-reforming and purification operations, instead of pure hydrogen, functional anode materials should be sought after in order to replace the conventional nickel oxide–yttria stabilized zirconia (NiO–YSZ) anode material. This is due to its high susceptibility to undergo coking during SOFC operation, resulting in a progressive electrochemical reaction inactivation [1]. However, mixed conductivity and fuel direct oxidation, or direct reforming electrocatalytic activities, also have to be guaranteed. Enhancement of oxygen ion storage and conductivity in the anode material is required to facilitate reaching those objectives. It was found that acceptor-doped ceria shows higher mixed ionic and electronic conductivities than yttria-stabilized zirconia (YSZ) in reducing atmospheres [2,3]. In fact, cerium oxide became an important component in automotive emissions-control catalysis where its ability to store and release oxygen is used to compensate for changes in the partial pressure of oxygen and maintain the stoichiometric oxygen-to-fuel ratio which is required for optimal catalyst performance [4–6]. This so-called oxygen storage capacity of ceria relies on the ability of the cerium cations to cycle between 4+ and 3+ oxidation states under oxidizing and reducing conditions, respectively [4–7]. These redox properties of ceria are known to be influenced by interactions with other metal oxides such as zirconia. Indeed, ceria supported on zirconia and mixed oxides of ceria and zirconia have higher oxygen storage capacity than ceria all alone. Additionally, interactions between ceria and alumina are important in automotive catalysts for which it has been shown that ceria can help to stabilize the surface area of the γ-Al_2O_3 support [4,8–10]. This stabilization results from the formation

* Corresponding author. Tel.: +55 21 2562 8791; fax: +55 21 2562 8791.
E-mail addresses: selma@labh2.coppe.ufrj.br (S.A. Venâncio), pmiranda@labh2.coppe.ufrj.br (P.E.V. de Miranda).

0272-8842/$36.00
doi:10.1016/j.ceramint.2011.05.054

of cerium aluminate ($CeAlO_3$) and its extent depends on a variety of factors including ceria dispersion, temperature and the gaseous environment. Likewise, the interest in interactions between ceria and zirconia may also be extended to solid oxide fuel cells where ceria finds usage as an anode oxidation catalyst that is in contact with the oxygen ion conducting electrolyte, YSZ [4,11–16]. Although reducing atmospheres enhances ceria's mixed ionic and electronic conductivities [17], its mechanical stability, which is a very important practical parameter, is not satisfactory under those conditions [18]. This has stimulated the search for a ceria-based functional SOFC anode material to which aluminum would be added as a way to enhance its mechanical properties without introducing harmful effects on its ionic conductivity, improving its thermal stability by benefiting from the high surface area of Al_2O_3 and introducing special anode electrocatalytic properties.

The present study has focused its attention towards the development of an SOFC anode electrocatalyst based on the binary ceria–alumina oxide, CeO_2–Al_2O_3, synthesized by the well-known and largely used amorphous citrate method [19], which has been widely used for the synthesis of doped and undoped aluminum and cerium oxides, among other oxide materials. The work was designed to determine the optimal conditions to synthesize such electrocatalysts in the form of nanometric ceramic powders. Furthermore, the study seeks to make them satisfy anode SOFC requirements by well understanding and controlling their phase transitions, crystalline structure during calcinations, particle size, morphology, density and purity in order to be well suited to produce ceramic suspensions. This approach was indeed effective, since the study has shown that the crystalline structure of the CeO_2–Al_2O_3 compound strongly depends on composition, temperature and atmosphere heat treatment.

2. Experimental procedures

2.1. $CeAlO_3$/CeO_2–Al_2O_3 synthesis

To synthesize the $CeAlO_3$/CeO_2–Al_2O_3 electrocatalyst, cerium nitrate [$Ce(NO_3)_3{\cdot}6H_2O$] and aluminum nitrate [$Al(NO_3)_3{\cdot}9H_2O$] solutions were used with an aqueous solution of citric acid ($C_8H_8O_7{\cdot}H_2O$). The methodology employed consists of the preparation of an initial solution containing the cations of interest with deionized water and an amount of citric acid such that for each equivalent-gram of citric acid there was a corresponding equivalent-gram of the metals for the completion of the cations. In this case, 1:1 metal:citric acid and 1:1 metal:metal (Ce:Al) molar relations were used. A cerium citrate solution was prepared under mechanical stirring using cerium nitrate and citric acid. The aluminum citrate solution was prepared in the same fashion. The cerium and aluminum citrate solutions were homogenized under mechanical stirring while the solution pH was made equal to 7 by the controlled addition of ammonia. The resulting solution was then heated to 75 °C and was subject to continual mechanical stirring in order to evaporate water and liberate NO_x, increasing its viscosity to form a gel. Total elimination of NO_x and formation of a resin was possible by increasing the heat to 90 °C.

The resin obtained was pre-calcined at 200 °C for 6 h in order to initiate the elimination of organic material. The resin then presented a black coloring and its X-ray spectrum was shown to be mainly constituted of $CeAlO_3$ with small CeO_2 peaks, as depicted in Fig. 1. The powders obtained were subsequently calcined at the temperatures of 300 °C, 400 °C, 600 °C, 800 °C and 900 °C. An additional condition consisted of calcining the sample at 900 °C and subsequently reducing it in hydrogen atmosphere for 6 h to acquire the desired crystalline structure. The samples prepared with these conditions were named CeAl3, CeAl4, CeAl6, CeAl8, CeAl9 and CeAl9RH, respectively. To confirm assumptions made based on the results obtained, supplementary treatments were performed with all samples at 1300 °C under an oxidizing atmosphere. For this reason, the suffix Tr13 was added to the previously mentioned sample nomenclature.

2.2. Methods

The thermal decomposition of the resin was analyzed by thermogravimetry (TG) and differential thermal analysis (DTA) which were simultaneously conducted in a TG8110 equipped RIGAKU TAS 100 equipment, using Al_2O_3 as reference material, by heating up to 1000 °C at a heating rate of 10 °C/min in an oxidant atmosphere introduced with an air flux of 70 mL/min. The specific surface area was determined by gaseous adsorption with the use of the Brunauer, Emmett and Teller (BET) technique in an ASAP2010-Micrometics equipment. The particle size distribution was calculated using the BET specific area data and Eq. (1) [20]:

$$D_{BET} = \frac{f}{\rho \times S} \quad (1)$$

where, D_{BET} is the particle average diameter, f is a shape factor (equal to 6 by considering the spherical particle), S is the

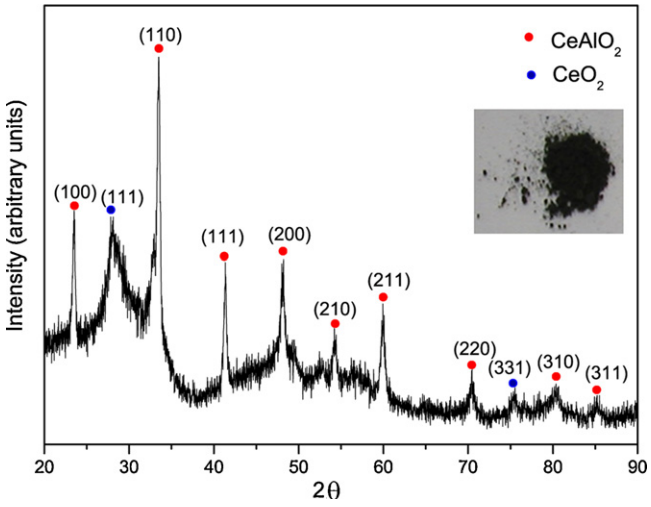

Fig. 1. X-ray diffraction spectrum of the as-synthesized powder, calcined at 200 °C. The insert presents a photograph of the ceramic powder.

powder specific surface area and ρ is the powder density calculated by Rietveld refining.

X-ray fluorescence analysis was conducted with the objective of identifying and to making a semi-quantitative determination of the chemical elements actually present in the electrocatalysts, also allowing for the evaluation of their respective levels of purity. An S4 Explorer model Bruker spectrometer equipped with Spectra Plus software was used to perform the before mentioned evaluation. Microstructural and morphological analyzes were performed with localized chemical element analysis by SEM, using a JSM-6460L JEOL microscope, and by TEM, making use of a model TECNAI 200-STEM, FEI microscope. Phase determination and crystalline structure were analyzed by an X-ray diffractometry in an XRD-6000 Shimadzu equipment, with Cu Kα radiation ($\lambda = 0.1506$ nm), varying coupled $\theta/2\theta$ between 20° and 90° (in 2θ) with a speed of 0.02° min^{-1}, acquiring data every 0.6 s. Diffraction patterns derived from the diffractograms were compared with PCPDF standard data file. The crystallite diameter ($D_{h\,k\,l}$) was determined by taking the average of the full width at half maximum (FWHM), with the aid of the FullProf software, of the five diffraction peaks with the highest magnitude of the predominant phase $CeAlO_3$ for samples CeAl3, CeAl4, CeAl6 and CeAl9RH and those of the predominant phase CeO_2 for the samples CeAl8 and CeAl9. Assuming the crystallites are strain free, their diameter was estimated by use of the Debye–Scherrer equation [21]:

$$D_{hkl} = \frac{\lambda \times K}{\beta \cos\theta} \quad (2)$$

where, λ is the (Cu Kα) radiation wave length, θ is the diffraction angle, K is a constant and β is the FWHM diffraction peak. The Rietveld scrutiny was carried out using the Rietveld analysis program package FullProf, which is also capable of doing a quantitative multi-phase analysis.

Raman spectra were collected with a System 1000 (Renishaw plc) microprobe. The power of the exciting laser light was about 1mW and the dispersed radiation was captured with a charge-coupled device. Raman spectrum of the examined oxides shows the relevant features in the range 0−1800 cm^{-1} (Raman frequency).

Sample density determination was done with an AccuPyc-1330 helium pycnometer from Micrometics. The sample weight was controlled using an analytical balance in order to occupy the approximate standard volume, equivalent to 1/3 of the equipment crucible volume. The measuring system was purged 15 times before operation and the final result was obtained from the average of the five respective readings. Temperature programmed reduction (TPR) was performed with sample CeAl9 using a Micrometics Pulse Chemisorb 2705 equipment, using a sample with a weight of 10 mg positioned in an U-tube type quartz reactor. The sample was dried under a helium flux of 15 mL/min at a heating rate of 10 °C/min up to 150 °C, for 30 minutes. After drying, a 30 mL/min flux of 10% H_2/Ar percolated the sample at 10 °C/min up to 1000 °C.

3. Results

3.1. Thermal analysis (TG and DTA)

Fig. 2 shows the results of the thermal decomposition of the resin. The exothermic peak at ∼280 °C is most likely related to the decomposition of the organic matter in the form of CO and CO_2. The result is in accordance with the previous results obtained from the other ceramic materials prepared with this same synthesis technique [22,23]. The TG curve shows initial mass loss between 25 °C and 150 °C equivalent to about 5% of the sample weight. The sample continuously lost weight until 280 °C. This is due to the elimination of both water and free citric acid within the resin [22,24], corresponding to approximately 65% of the sample weight loss that confirms the resin's hygroscopicity already observed by other researchers [25]. From there on, the oxide becomes stable with respect to weight loss and enthalpic reactions. The compounds prepared by the complexion of cations with citric acid may present two types of thermal decompositions: continuous (type I) or with an intermediate step, for which a complex is formed and the decomposition of a fraction of free citric acid takes place (type II). The main difference between the two types of decomposition lays on the thermal stability of the metallic citrate that is produced during the loss of nitrates from the solution [22,25].

The analysis of the DTA curve shows that from about 90 °C to 250 °C the variation in released energy might have occurred due to the following: (1) the vaporization of nitrates contained in the precursors; (2) the combustion of the organic matter; and (3) the release of CO_2. Within the range of temperature from 290 °C to 400 °C, a possible onset of the $CeAlO_3$ conversion to other oxides takes place with cerium being oxidized from Ce^{3+} to Ce^{4+}, generating an exothermic peak at a maximum of nearly 320 °C. The TG and DTA results shown supported the decision to prepare samples submitted to calcinations at temperatures equal to and greater than 300 °C.

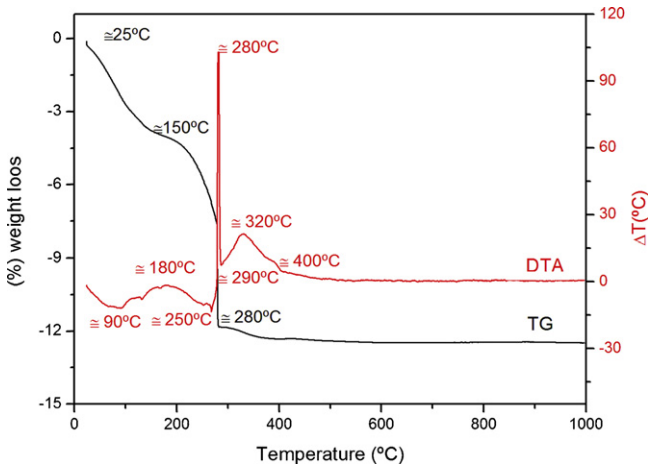

Fig. 2. TG and DTA curves for the resin obtained in the synthesis process.

3.2. Microstructural features

3.2.1. Visual and SEM analysis

A detailed analysis of the synthesized electrocatalytic powders was performed to study the morphology of the product obtained and the phase changes that took place during the different calcinations. Initial visual observation was followed by a thorough SEM analysis of all samples, as depicted in Fig. 3. The product left in the alumina crucible after calcinations in air at 300 °C (Fig. 3(a)) presents a predominate green color (For interpretation of the references to color in the text, the reader is referred to the web version of the article.). However, yellow particles are also visible, indicating that the material might be composed of two different compounds. These compounds are most likely to be $CeAlO_3$ and CeO_2 as a result of particle surface oxidation [26]. For the two subsequent calcination temperatures (400 °C and 600 °C, Fig. 3(b and c), respectively) under the oxygen rich atmosphere the powders

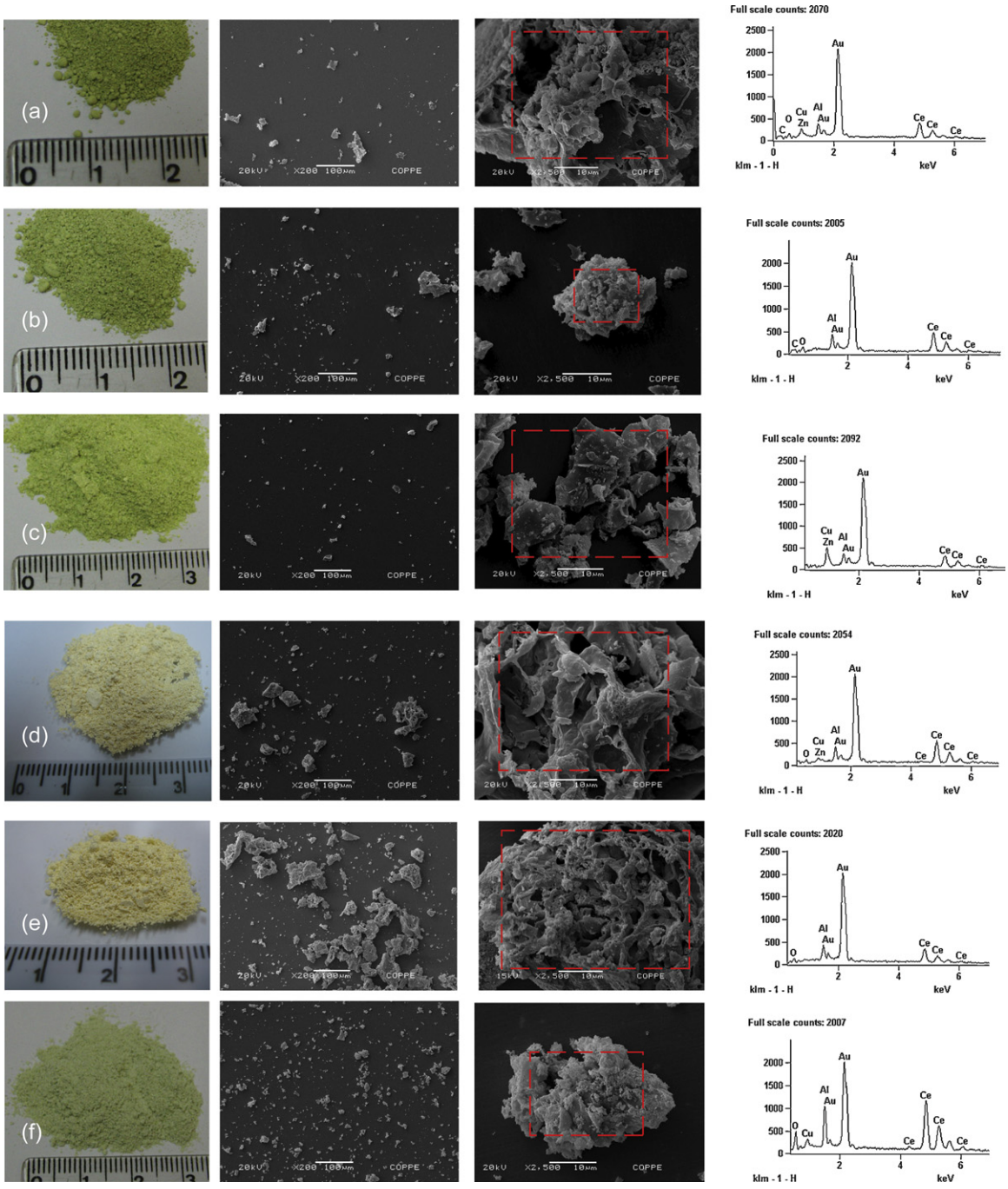

Fig. 3. Visual observation by macroscopic photography, as well as SEM microstructure morphology analysis and qualitative chemical analysis by dispersive energy (over the inner area of the dashed-lined square on the micrograph) are presented for each sample type, including (a) CeAl3; (b) CeAl4; (c) CeAl6; (d) CeAl8; (e) CeAl9 and (f) CeAl9RH. Original magnifications of the SEM micrographs shown are equal to 200× (left hand side micrograph) and 2500× (right hand side micrograph).

present the same feature of green and yellow particles, though the presence of the latter is progressively present. For the calcinations in air performed at higher temperatures of 800 °C and 900 °C (Fig. 3(d and e), respectively), the powder appears in the color of a pale yellow, indicating a probable predominant presence of the CeO_2 phase. By calcinating a sample such as that shown in Fig. 3(e), at 900 °C for 6 h under a reducing hydrogen atmosphere, the powder once again becomes green colored (Fig. 3(f)), indicating a probable predominant presence of the $CeAlO_3$ phase. SEM morphological analysis showed that in all cases a wide range of size distribution of weak agglomerates is encountered. As higher magnifications are employed, the weak agglomerates present themselves with the aspect of irregular and heterogeneous sponges, which are indeed fragile being easily torn apart into smaller agglomerates. Such porous structure is attributed to the important evolution of gases during the citrates synthesis process, which is not apparently affected by the increase in calcination temperatures. SEM dispersive energy spectra were also obtained in each case and are presented in Fig. 3. The presence of the main chemical elements expected to constitute the powder particles, Ce, Al and O, are confirmed and Au, Cu and Zn peaks are due to SEM sample pre-coating with gold and to the sample holder, respectively.

3.2.2. TEM analysis

Searching for a deeper understanding of the particles' morphology, a transmission electron microscopy (TEM) analysis was performed, as depicted in Fig. 4. The sequence of TEM micrographs for all samples illustrated in Fig. 4 unveils a similar dimensional structure for the particles in sample CeAl3 and sample CeAl4, presenting similarities in size and shape. Continuing from sample CeAl6, very small supported particles with sizes ranging from 5 nm to 10 nm began to appear when calcined at 600 °C. In samples CeAl8 and CeAl9 this effect is enhanced, but these small supported particles grow in size to reach diameters in the ranges of 7–12 nm and of 13–22 nm, respectively. Moreover, it can be rationalized and inferred that the tiny supported particles observed are CeO_2 crystallites that grow on top of the $CeAlO_3$ phase with the increase in temperature upon calcinations in the air.

3.2.3. X-ray fluorescence chemical analysis

A semi-quantitative analysis of the Ce and Al chemical elements present in each electrocatalyst after being calcined at the reference temperatures was performed via X-ray fluorescence spectrometry (XRF). This analysis negated the presence of any other metallic elements other than Ce and Al. Table 1 presents the value of these chemical elements in terms of weight percentage or in molar concentrations. The average value for the Ce to aluminum molar proportion (Ce:Al) deviates from the expected 1:1 relation to slightly greater cerium amounts for all samples, including the sample in an atmosphere of reduced hydrogen, CeAl9RH. These results also show that the weight percentage of cerium is, naturally, found to be greater than an approximate 80:20 Ce:Al expectable proportion. One may observe that the molar concentrations do not vary significantly with the variation of the sample calcination temperature, indicating that the overall chemical composition is not greatly modified with the increase of the calcination temperature.

3.2.4. X-ray diffraction analysis and rietveld refinement

The X-ray diffraction patterns obtained in each of the sample types are shown in Fig. 5, where the peaks for each crystalline phase present are marked° for CeO_2 and * for $CeAlO_3$. It may be noted that the powder calcined in air at temperatures of up to 600 °C mostly present peaks corresponding to the $CeAlO_3$ phase, together with a few low-intensity peaks of CeO_2. By increasing the temperature to more than 600 °C, the peaks corresponding to CeO_2 are more noticeable and clearly defined. For the powders calcined at 800 and 900 °C mainly CeO_2 is present. Most of the $CeAlO_3$ peaks are either very close to or superimposing with those corresponding to CeO_2, except for the (1 0 0) and (1 1 1) $CeAlO_3$ peaks that show up on $2\theta = 23.5^\circ$ and $2\theta = 41.4^\circ$, respectively. It is striking, though, that there is apparently no formation of Al_2O_3, as detected by the X-ray diffraction analysis. Considering that Al_2O_3 is present in significant proportions in the components used to synthesize the powders, it is surprising to find only CeO_2 and $CeAlO_3$ in the samples analyzed.

Furthermore, all samples calcined in air at higher temperatures are well oxidized, but no Al_2O_3 was found despite the fact that the metal aluminum constitutes on average about 44.35% of the metallic molar fraction of the alloy (as depicted in Table 1) and that the determination of the atomic proportion of the metals present in the samples at the end of the synthesis yielded about 16% aluminum. Based on those findings, one would presume that aluminum oxide is present in the samples, but cannot be easily detected. Possible reasons for this include difficulties to detect alumina (even knowing that it may possess four different crystalline structures), for its peaks being superimposed with ceria's; or by taking into account that the enormous difference in atomic weights of cerium and aluminum, 140.12 g and 26.98 g, respectively, would present the cerium peaks in such an important intensity that the aluminum peaks could not be easily identifiable; or by considering that aluminum oxide is in an amorphous state, hindering its detection by the experimental methods used.

Aluminum oxide Al_2O_3 undergoes a sequence of structural transformations from γ-Al_2O_3 to its more stable form α-Al_2O_3 as follows: $\gamma \rightarrow \delta \rightarrow \theta \rightarrow \alpha$. It is known [27] that the stability of a certain alumina phase is dependent on the reaction conditions during the synthesis process. An example cited was the use of a particular fuel in the Al_2O_3 combustion synthesis, hexamethylenetetramine, resulting in the formation of amorphous Al_2O_3. However, by adding an additional oxidant such as NH_4ClO_4, it crystallized into α-Al_2O_3 [27–30]. This takes place due to the combination of a strong oxidant agent and a reducing fuel, giving origin to a strong exothermic reaction with the consequent increase in temperature that facilitates Al_2O_3 crystallization. Moreover, for a given fuel, when there is more than one phase present, the phase stability depends on the composition of the mixture. In the present case, when the

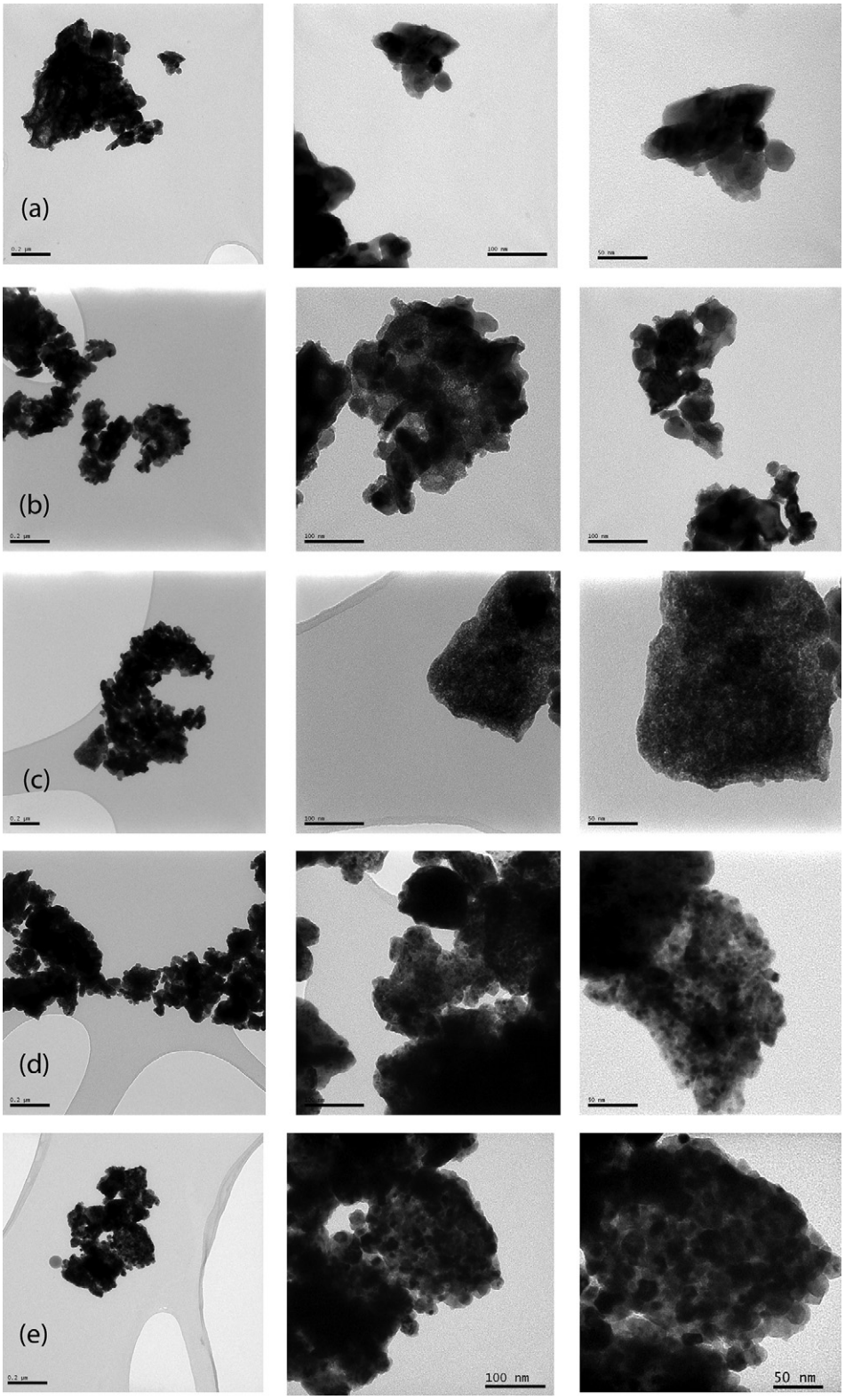

Fig. 4. Transmission electron micrographs for the samples: (a) CeAl3; (b) CeAl4; (c) CeAl6; (d) CeAl8; and (e) CeAl9.

samples were synthesized in the form of nanoparticles, the components of the binary system CeO_2–Al_2O_3 delayed each other's crystallization process. Then, the presence of CeO_2 in the binary system may hinder the crystallization of the aluminum oxide. In other words, when alumina is present, the synthesis thermal energy is preferably used to crystallize ceria [27,28].

Several dissimilar crystalline structures have been reported for $CeAlO_3$ [26,31–36]. Past structural studies showed that the material was composed of a tetragonal unit cell with lattice

Table 1
X-ray fluorescence data for the electrocatalysts studied.

Sample	Ce (%wt/wt)	Al (%wt/wt)	Ce (mol%)	Al (mol%)
CeAl3	87.00	13.00	56.30	43.70
CeAl4	86.50	13.50	55.23	44.77
CeAl6	86.00	14.00	54.20	45.80
CeAl8	86.4	13.6	54.95	45.05
CeAl9	87.44	12.4	57.59	42.41
CeAl9RH	87.2	12.8	56.75	43.25

parameters equal to $a = 0.3760$ nm and $c = 0.3787$ nm [31]. Subsequently, other configurations were proposed, including a rhombohedral unit cell with $a = 0.5327$ nm and $\alpha = 60{,}25^{\circ}$ [32]; a primitive tetragonal cell with $a = 0.3763$ nm and $c = 0.3792$ nm and an orthorombic cell with $a = 0.5316$ nm, $b = 0.5314$ nm and $c = 0.7576$ nm [26]. Furthermore, citations considering hexagonal, trigonal and cubic unit cells for the $CeAlO_3$ lattice have also been reported in literature [33,34]. These structural uncertainties occur possibly due to the structure symmetry and because of small distortions caused by the inclination of the AlO_6 octahedrons [34,35]. The two structures that are most widely accepted for $CeAlO_3$ are: (1) a primitive tetragonal cell with P4/mmm space group and lattice parameters equal to $a = 0.37669$ nm and $c = 0.37967$ nm [33,35] and (2) a body centered tetragonal unit cell with I4/mcm space group and lattice parameters equal to $a = 0.532489$ nm and $c = 0.758976$ nm [26,34,35].

Rietveld refinement analyzes were conducted for all samples in order to make detailed studies of their already mentioned crystalline structures for which profiles were adjusted with a pseudo-Voigt function. Fig. 5 also presents the Rietveld graphics plotted for each sample type. The refined lattice parameters determined for the main $CeAlO_3$ phase that presented a primitive tetragonal cell with space group P4/mmm were equal to: $a = b = 0.37758$ nm and $c = 0.37740$ nm for sample CeAl3; $a = b = 0.37652$ nm and $c = 0.37333$ nm for sample CeAl4; $a = b = 0.37979$ nm and $c = 0.37644$ nm for sample CeAl6; and $a = b = 0.37719$ nm and $c = 0.37730$ nm for sample CeAl9RH. On the other hand, the refined lattice parameters for the CeO_2 phase, the main phase contained in samples CeAl8 and CeAl9, that presented a cubic unit cell with space group FM-3m, were equal to $a = 0.54112$ nm and $a = 0{,}5{,}4157$ nm, respectively. The data displayed above may be compared to those from the literature equal to $a = 0.54113$ nm for CeO_2 and $a = 0.3773$ nm and $c = 0.37967$ nm for $CeAlO_3$ [27].

Tables 2 and 3 present the Rietveld refinement results for the $CeAlO_3$ phase with space group P4/mmm observed in sample CeAl9RH as well as the results of the CeO_2 phase with space group FM-3m present in sample CeAl9. In both cases the total number of parameters refined was equal to 43 points.

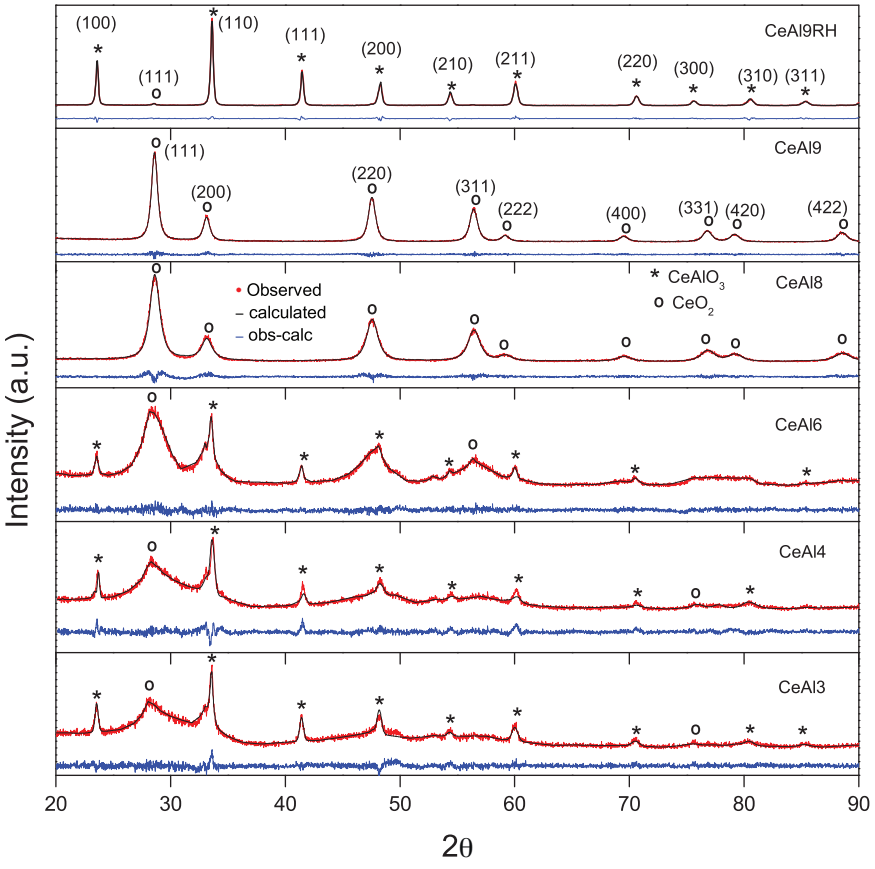

Fig. 5. X-ray diffraction spectra and Rietveld observed and computed diffraction patterns determined for powder samples CeAl3; CeAl4; CeAl6; CeAl8; CeAl9 and CeAl9RH. The X Ray peaks for CeO_2 are identified by open circles and those for $CeAlO_3$ by asterisks.

Table 2
Structural parameters for the $CeAlO_3$ phase with tetragonal unit cell and space group P4/mmm present in sample CeAl9RH.

Atoms	Type	Position	x	y	z	B_{iso}
Ce	Ce^{3+}	1d	0.53904	0.50000	0.44082	0.20222
Al	Al^{3+}	1a	0.00000	0.00000	0.00000	0.24000
O (1)	O^{2-}	2f	0.50000	0.75708	0.00000	0.59000
O (2)	O^{2-}	2f	0.27317	0.50000	0.00000	0.73000
O (3)	O^{2-}	1b	0.00000	0.00000	0.50000	0.74000

R_{wp} = 16.7; R_p = 14.4, S = 1.713 B_{iso} = isotropic atomic displacement.

It is worth mentioning that the Rietveld refinement yielded satisfactory results. In convergence, the agreement factors were R_{wp} = 16.7 and R_p = 14.4, with Goodness-of-fit (S) equal to 1.713 for $CeAlO_3$. For the CeO_2 phase the agreement factors were R_{wp} = 17.37 and R_p = 14.4, with Goodness-of-fit (S) equal to 1.875. B_{iso} stands for the isotropic atomic displacement.

The crystallite size $D_{h\,k\,l}$ determined using Eq. (2) for sample types CeAl3, CeAl4 and CeAl6 were 31.75 nm, 30.22 nm and 17.33 nm, respectively. These crystallite sizes are related to the $CeAlO_3$ phase. The decrease in size of the crystallite coupled with the increase in the calcination temperature is possibly related to the progressive reduction of the mass fraction of $CeAlO_3$ and the increased crystallization of the CeO_2 phase. Since the CeO_2 diffraction peaks present low intensity and are not precisely defined in these samples, their crystallite grain size was not determined. The crystallite sizes for the $CeAlO_3$ and CeO_2 phases that are present in the hydrogen reduced sample, CeAl9RH, are equal to 64.20 nm and 28.00 nm, respectively.

The crystallite sizes, $D_{h\,k\,l}$, determined for CeO_2, the main crystalline phase present in samples CeAl8 and CeAl9, were equal to 7.65 nm and 13.70 nm, respectively. From those measurements, one may conclude that the fabrication procedure used yielded oxides with nanometric sized crystallites, for which the CeO_2 crystallites are much smaller than the $CeAlO_3$ crystallites. As expected, the increase in calcination temperature contributes to the growth of such crystallites that are also observable when the powders are retreated for the reduction procedure with hydrogen at 900 °C. It is worth pointing out that in all diffraction patterns obtained, the peaks corresponding to the $CeAlO_3$ phase are narrower, more intense and better defined, indicating the high level of crystalline character in this phase.

3.3. Density considerations

With the goal of evaluating the electrocatalyst powder particle morphology, their density and porosity, helium pycnometry measurements were performed with all sample types (CeAl3; CeAl4; CeAl6; CeAl8; CeAl9 and CeAl9RH). These results were coupled with the X-ray diffraction determinations for the phase type, unit cell volume and phase concentration to compile the data presented in Table 4. This data was used to calculate the sample density and to compare it with the experimentally determined density value by pycnometry. The fact that samples type CeAl3, CeAl4, CeAl6 and CeAl9RH contain two crystalline phases, the tetragonal perovskite-type $CeAlO_3$ and the cubic fluorite-type CeO_2 phase, as indicated by the X-ray diffraction analysis performed, were taken into consideration upon determining the sample densities. The density ρ yielded from the X-ray data is expressed as:

$$\rho = \frac{M \times 10^{24}}{V \times 6.023x10^{23}} \quad (3)$$

where M is the molecular mass and V the unit cell volume. The density calculated by weighting out the proportions of the phases present, ρ_c, is given by:

$$\rho_c = \frac{\rho_1 \times \rho_2}{\rho_2 \boldsymbol{X}_{m1} + \rho_1 \boldsymbol{X}_{m2}} \quad (4)$$

where ρ_1 and ρ_2, $\boldsymbol{X}_{m1}$ and $\boldsymbol{X}_{m2}$ are, respectively, the densities and the molar fractions of phases 1 and 2.

The experimental density values determined by pycnometry are smaller but very close to the density values calculated using the X-ray diffraction data. Density values found for $CeAlO_3$ are fairly compatible with data previously recorded [36], equal to 6.64 g/cm^3, considered to possess a tetragonal unit cell with space group I4/mcm. The calculated density values herein shown for CeO_2 are also compatible with the one obtained with the data from PCPDF (43-1002), equal to 7.215 g/cm^3.

The data from Table 4 for the samples calcined at temperatures up to 600 °C show an increase in the electrocatalyst density and a decrease in porosity. This result was indeed expected since the porosity decreases as the as organic residues are eliminated with the increase on the calcination temperature. However, with an increase in calcination temperature, such as 800 °C and 900 °C, the values of the calculated densities increased due to the predominant presence of the CeO_2 phase, but the experimentally determined densities are somewhat smaller than expected due to the increased porosity observed. The latter is potentially caused by misalignments originated in the process of phase transformations. The density value found for the CeAl9RH type sample is very much compatible to that of the as synthesized sample, both containing the basically $CeAlO_3$ phase. The smaller experimentally determined density, as compared to calculated density for the hydrogen reduced sample, is compensated by its increase in porosity.

Table 3
Structural parameters for the CeO_2 phase with cubic unit cell and space group FM-3m present in sample CeAl9.

Atoms	Type	Position	x	y	z	B_{iso}
Ce (1)	Ce^{4+}	4a	0.00000	0.00000	0.00000	0.29000
O (1)	O^{2-}	8c	0.25000	0.25000	0.25000	1.82000

R_{wp} = 17.4; R_p = 14.4; S = 1.875; B_{iso} = isotropic atomic displacement

3.4. Surface area analysis

The specific area of all sample powders was determined by BET to better understand the phases' segregation during synthesis and also as a means to evaluate their stability,

Table 4
X-ray-based and pycnometry measurements based density values determination for the electrocatalysts produced.

Sample/ phase	Unit cell volume (nm^3)	Phase concentration (%)	Density – calculated (g/cm^3)	Density – experimental (g/cm^3)	Volume of pores ($cm^{3)}$
CeAl3					
$CeAlO_3$	5.8805	99.72	6.07	6.06 ± 0.1575	0.124 ± 0.0028
CeO_2	15.8551	0.28			
CeAl4					
$CeAlO_3$	5.2927	99.21	6.76	6.09 ± 0.0429	0.116 ± 0.0007
CeO_2	13.6308	0.79			
CeAl6					
$CeAlO_3$	5.4299	70.36	7.05	7.04 ± 0.1896	0.075 ± 0.0002
CeO_2	15.7170	29.64			
CeAl8					
CeO_2	15.8245	100	7.21	7.14 ± 0.0285	0.1865 ± 0.0009
CeAl9					
CeO_2	15.8392	100	7.21	7.19 ± 0.1588	0.1941 ± 0.0020
CeAl9RH					
$CeAlO_3$	5.3680	98.71	6.01	5.75 ± 0.5472	0.998 ± 0.031
CeO_2	15.8841	1.29			

The phase concentration values shown in table may be affected by other parameters analyzed in Section 4.

chemical reactivity and other materials properties. Upon determination of the specific area values, Eq. (1) was used to calculate the powder (D_{BET}) particle sizes as resulted from each calcination temperature treatment. Table 5 presents these data together with the crystallite sizes obtained by treating the X-ray data of the predominant crystalline phase with the Rietveld refinement method. The specific area decreases progressively with the increase on the calcination temperature, which indicates that the particle size is increasing. This is expected by the probable coalescence of particles resultant from the higher temperature treatments. However, the phase transitions and the variation on the degree of crystallinity affect these data, as depicted by the crystallite sizes calculated. These are rather coincident with the particle sizes measured at the lower calcination temperatures, but are very much affected by the above mentioned factors at the higher calcination temperatures.

3.5. TPR analysis

The hydrogen induced reduction of CeO_2 takes place initially on the surface to progressively affect the volume of the material in continuation. Because of that, this phenomenon is highly sensitive to the sample surface area and experiences bulk reduction as the surface active sites are consumed, being favored by the high mobility of oxygen in the CeO_2 lattice.

Table 5
Specific area and particle size.

Sample	Specific area ($m^2\ g^{-1}$)	D_{BET} (nm)	$D_{h\ k\ l}$ (nm) (predominant phase)
CeAl3	34.0 ± 0.0243	29.0	31.75($CeAlO_3$)
CeAl4	28.9 ± 0.2119	30.7	30.22($CeAlO_3$)
CeAl6	22.1 ± 0.1251	38.5	17.33($CeAlO_3$)
CeAl8	17.3 ± 0.0313	48.1	7.65(CeO_2)
CeAl9	16.8 ± 0.0037	49.5	13.70(CeO_2)
CeAl9RH	7.4 ± 0.0026	134.9	64.20($CeAlO_3$)

Upon searching for a deeper understanding of the CeO_2 reduction mechanisms, sample CeAl9 was submitted to temperature programmed reduction (TPR) analyzes. Fig. 6 depicts the H_2-TPR profile for the CeAl9 sample that presents a unique reduction region for which the hydrogen consumption peaks at approximately 920 °C. This high temperature peak is associated with the reduction of Ce^{4+} to Ce^{3+} as $CeAlO_3$ is formed, as shown by the X-ray diffraction data (Fig. 5) and supported by literature [37]. It is reported [37] that the reduction of the original oxides CeO_2/Al_2O_3 begins to take place at temperatures above 800 °C and corresponds to removing oxygen from the bulk. The high temperature might favor the interaction between cerium oxide species and alumina. During the reduction procedure surface cerium ions are reduced from Ce^{4+} to Ce^{3+} and new types of interactions between these ions and alumina may be considered to form

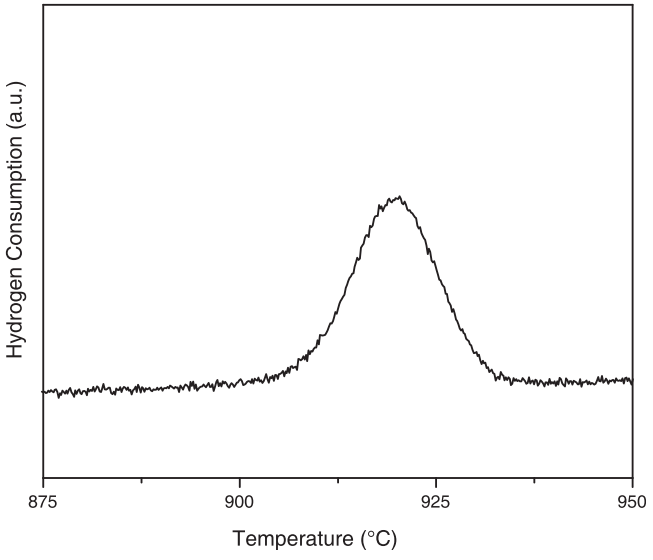

Fig. 6. H_2-TPR profile obtained for the sample type CeAl9 heat treated at 900 °C.

$CeAlO_3$ by occupation of the Al^{3+} cationic sites by Ce^{3+} cations. According to Humbert et al. [37], the occurrence of $CeAlO_3$ results from the diffusion of Al^{3+} into the partially reduced CeO_2 lattice, allowing for the quick diffusivity that is aided by the small ionic diameter of Al^{3+} compared to that of Ce^{3+} (0.050 nm and 0.103 nm, respectively) [38,39].

In the present work, the reduction of CeO_2/Al_2O_3 to $CeAlO_3$ was also followed by a variation on the sample's color appearance that changes from pale-yellow to pale-green, as depicted in Fig. 2. This statement is supported by the X-ray diffraction analysis results presented in Fig. 4. The presence of small amounts of CeO_2 after reduction may be caused by the formation of Ce_x containing phases, such as Ce_2O_3, because the reduction temperature is above 800 °C upon the nucleation of $CeAlO_3$ from CeO_2 and Al_2O_3. Some Ce_x-type oxides may form solid solutions in alumina and the remaining species are re-oxidized when exposed to air. It seems that the formation of $CeAlO_3$ from CeO_2 in alumina involves an intermediate state in which ceria is partially reduced.

4. Discussion

One of the main points chosen to be further discussed regarding the results presented in the paper is the absence of alumina in all X-ray diffraction crystallographic analysis made of the samples in the oxidized state, in particular the one treated in air at 900 °C, sample type CeAl9. This motivated the design of a high temperature heat treatment for CeAl9 sample type under an oxidizing atmosphere (1300 °C in air for 6 h), following indication from the literature [40] that crystalline α-Al_2O_3 is supposed to be observed in this condition. Hence, this heat treatment was intended to evaluate the stability of the electrocatalyst developed and also to confirm if the crystalline Al_2O_3 phase would not be observed since it had not been detected in any of the previous samples that underwent air calcination treatments in different temperatures. Fig. 7 presents

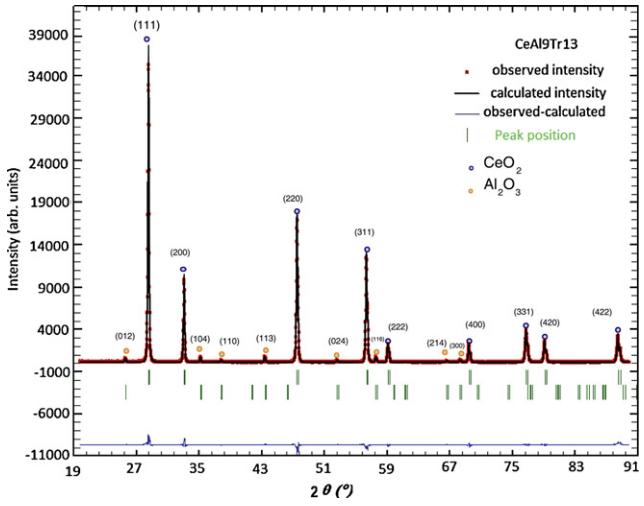

Fig. 7. X-ray diffraction spectrum and Rietveld observed and computed diffraction pattern results determined for the powder sample CeAl9Tr13 that was heat treated in air at 1300 °C for 6 h after being prepared as a CeAl9 sample type.

the X-ray diffraction patterns for a sample type CeAl9 heat treated in air at 1300 °C, which hereafter will be named CeAl9Tr13. The X-ray diffraction peaks corresponding to the Al_2O_3 phase are clearly observed in Fig. 7 in addition to the peaks corresponding to CeO_2. A quantitative analysis of the phases present was made using the Rietveld method, yielding a mass fraction of CeO_2 equal to 77.07% and a mass fraction of Al_2O_3 equal to 22.93%. Application of the Rietveld refinement procedure was considered satisfactory, yielding R factors such as $R_{wp} = 9.23$ and $R_p = 7.60$ and an S factor equal to 1.49. The refined lattice parameters for Al_2O_3, considering a rhombohedric unit cell with space group R-3C, were $a = b = 0.47552$ nm and $c = 1.29830$ nm. The refined lattice parameters for CeO_2, with a cubic unit cell and space group FM-3 m, were $a = b = c = 0.54107$ nm. The observed and computed X-ray diffraction patterns for this system are also illustrated in Fig. 7. These findings have undoubtedly shown that heat treatment at a higher temperature under oxidizing conditions yields an important amount of crystalline Al_2O_3 phase.

It would then be important to utilize another rational to identify if amorphous alumina would be present in the constitution of the samples evaluated in the present work, especially the samples fully oxidized at 900 °C, such as sample type CeAl9.

Initially, an analysis is made of the synthesis procedure used to obtain the ceramic powders in which $CeAlO_3$ is the main component obtained. While in CeO_2 the cerium stable oxidation state is 4+, in $CeAlO_3$ it is 3+, requiring immersion in a highly reducing atmosphere to be formed. Such a reducing atmosphere is created by blending citric acid and ammonia in the synthesis procedure.

In fact, it was experimentally demonstrated that the following reaction is reversible:

$$4CeAlO_3 + O_2 \leftrightarrow 4CeO_2 + 2Al_2O_3 \quad (5)$$

That is, at suitably high temperatures $CeAlO_3$ may be oxidized to CeO_2 and Al_2O_3 upon being heated under air, whereas CeO_2 and Al_2O_3 may be reduced to $CeAlO_3$ upon being heated under a hydrogen atmosphere. This is demonstrated in Fig. 5 where intense $CeAlO_3$ peaks are observed for sample CeAl9RH and in Fig. 7 where CeO_2 and Al_2O_3 peaks are observed for sample CeAl9Tr13. However, although crystalline Al_2O_3 was easily detected and quantified in sample type CeAl9Tr13, this oxide was not identified by X-ray diffraction in any other sample type. In fact, the cation order–disorder and the crystalline lattice distortion may, in principle, be easily detected by conventional X-ray diffraction analyzes, but it is not able to precisely detect oxygen sub-lattice distortions or structural defects due to the weak sensitivity of this technique for oxygen atoms in the presence of heavier atoms such as Ce and Al. Since the mobility of oxygen atoms in the lattice is a fundamental property for such an ionic–electronic conductor material, it is wise to deeply investigate these structural details. The Raman spectroscopy comes out as a powerful technique for such a procedure and Raman spectra were obtained for sample types CeAl9, CeAl9RH and

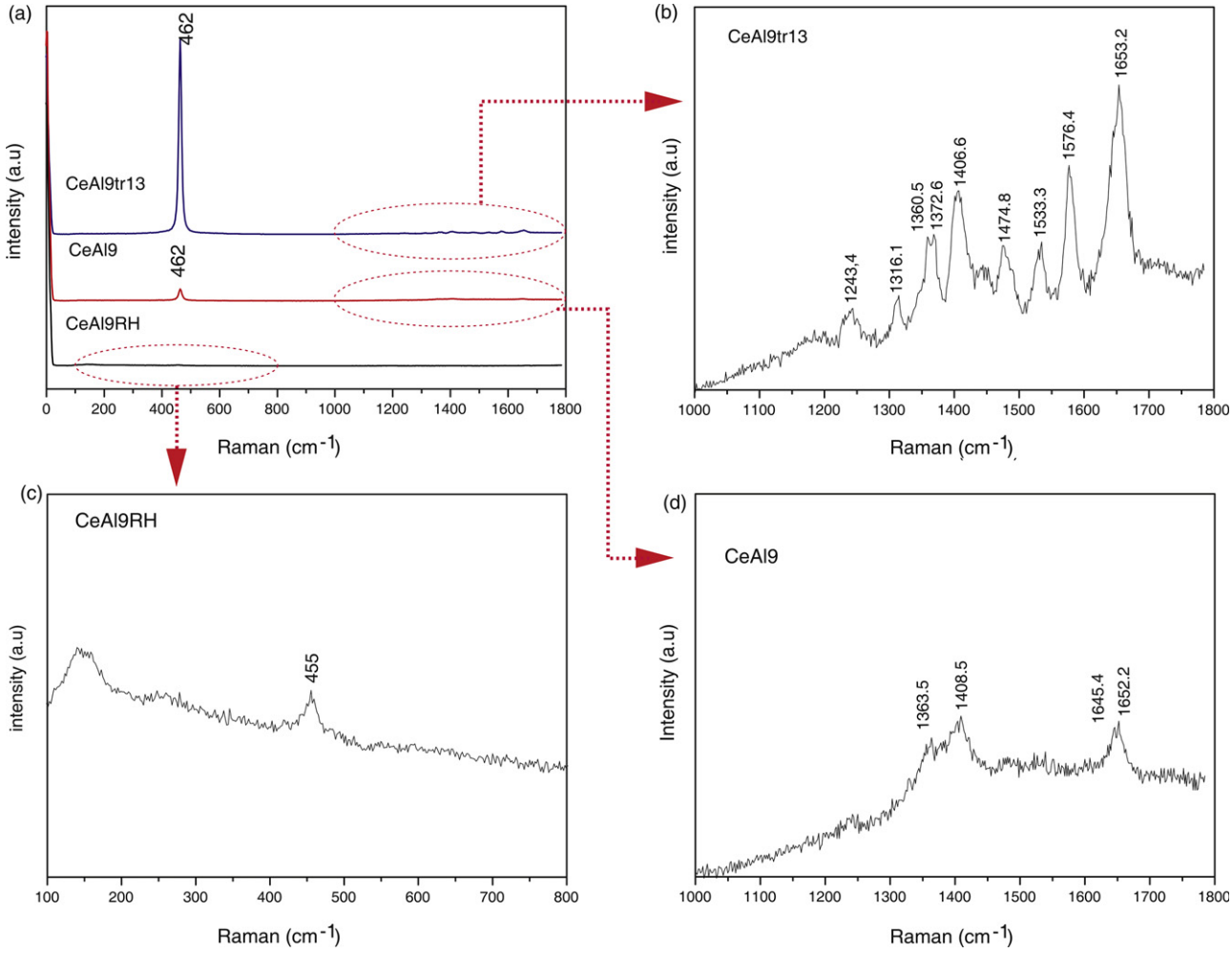

Fig. 8. (a) Raman spectra for the electrocatalyst powders corresponding to samples type CeAl9RH, CeAl9 and CeAl9Tr13. Amplification of the Raman spectra for the electrocatalyst: (b) CeAl9Tr13; (c) CeAl9RH and (d) CeAl9.

CeAl9Tr13, as depicted in Fig. 8. The CeAl9RH sample is in a reduced condition, in which $CeAlO_3$ is likely to be observed. It presents a perovskite type structure, slightly more distorted than the simple cubic perovskite one. However, the nature of these distortions is not totally understood. Although the deviation from the simple cubic structure is very small, the precise location of the atoms in the unit cell is unknown. For a cubic perovskite structure there are no Raman active vibration modes. For a $BaTiO_3$ type tetragonal structure, there would be eight Raman active modes: $T = 3A_1 + B_1 + 4E$ [31]. For a $LaAlO_3$ type rhombohedric structure, one may find five Raman active modes: $T = A_{1g} + 4E_g$ [10]. Hence, due to the very small distortion of the cubic structure, all Raman modes are very week. In fact, clear Raman spectra were not observed for the present results, concerning sample type CeAl9RH, in which the major component is $CeAlO_3$. Only a week intensity enlarged band was observed with wavelength number between 37.75 cm^{-1} and 230.21 cm^{-1}, as shown in Fig. 8(c), presenting an amplification of the corresponding spectrum shown in Fig. 8(a). Consistent to what was shown by the X-ray diffraction results, this spectrum depicts a low intensity band with wavelength number approximately equal to 455 cm^{-1} that might be indicating the presence of a mixture of $CeAlO_3$ and CeO_2. In fact, the main band, at the wavelength number 462 cm^{-1}, characteristic of the CeO_2 phase, was displaced to the wavelength number 455 cm^{-1}. This is an indication of the introduction of Al_2O_3 in the CeO_2 lattice to form $CeAlO_3$ upon being submitted to a reducing atmosphere.

Samples CeAl9 and CeAl9Tr13 are in the oxidized condition, the latter being fully oxidized and crystallized. The Raman spectra obtained for the oxidized samples are characterized by a high intensity band at the wavelength number 462 cm^{-1}, typical of the CeO_2 fluorite type structure [41]. This is assigned to the active Raman symmetry mode F_{2g}, which is threefold degenerated, associated to the vibration of oxygen atoms around the Ce^{4+} cations. This represents a symmetric Raman mode, known as ‘‘respiration mode’’ or ‘‘expansion–contraction’’ mode of the oxygen atoms around each cerium atom. Greater symmetry is found in the band at the wavelength 462 cm^{-1} for sample type CeAl9Tr13 than that of sample type CeAl9. This occurs because of the superior crystallization of ceria with increasing heat treatment temperature, as confirmed by the X-ray diffraction analysis. One must take into account that the evolution of the main

Table 6
X-ray-based and pycnometry measurements based density values determination for the electrocatalysts produced and heat treated at 1300 °C.

Sample/phase	Unit cell volume (nm^3)	Phase concentration (%)	Density – calculated(g/cm^3)	Volume of pores (cm^3)	Parameters Gof
CeAl3Tr13					
CeO_2	15.839	78.07 ± 0.41	6.12	0.124 ± 0.0028	1.63
Al_2O_3	25.4363	21.93 ± 0.51			
CeAl4Tr13					
CeO_2	15.8288	76.76 ± 0.55	6.08	0.116 ± 0.0007	1.95
Al_2O_3	25.3710	23.24 ± 0.33			
CeAl6Tr13					
CeO_2	15.8404	78.00 ± 0.39	6.12	0.075 ± 0.0002	1.74
Al_2O_3	25.4260	22.00 ± 0.52			
CeAl8Tr13					
CeO_2	15.8448	77.74 ± 0.44	6.11	0.1865 ± 0.0009	1.52
Al_2O_3	25.4370	22.26 ± 0.39			
CeAl9Tr13					
CeO_2	15.8405	77.07 ± 0.25	6.09	0.1941 ± 0.0020	1.49
Al_2O_3	25.4238	22.93 ± 0.21			

Raman bands is strongly dependent on the distribution of the size of the particles. Bands presented in a wide and asymmetric format may be related to the existence of a heterogeneous strain. Conversely, defined and symmetric bands indicate enhanced crystallization of the CeO_2 phase.

Fig. 8(b and d) present magnifications of the Raman spectra from Fig. 8(a), for samples CeAl9Tr13 and CeAl9, respectively. This was done in order to investigate the presence of alumina, capitalizing on an important advantage of the Raman technique over the conventional X-ray diffraction analysis: the possession of a higher intensity of the luminescent signal that allows to discriminate useful information about the presence of Al_2O_3 even if it is present in small quantities and/or with low level of crystalline character.

This approach is particularly suitable to follow the evolution of the alumina phase as the temperature of the heat treatment is increased. For example, two groups of signals are unveiled in Fig. 8(d) for the sample treated at 900 °C, CeAl9, in the range of the wavelength numbers between 1363.5 and 1408.5 cm^{-1} and between 1645.4 and 1652.2 cm^{-1}, being attributed to Al_2O_3 which was undetectable by the X-ray diffraction analysis. Increasing the sample heat treatment temperature to 1300 °C, sample type CeAl9Tr13, was sufficient to make the alumina phase to become clearly detectable by the conventional X-ray diffraction analysis, as shown in Fig. 7. This is compatible with what is shown by the Raman spectra of Fig. 8(b) by the bands in the wavelength numbers ranging from 1243.4 to 1653.2 cm^{-1} that correspond to the intense crystalline level of the alumina phase resulting from the heat treatment at 1300 °C.

Table 6 condenses the main results obtained after the appropriate corrections, weighing out the percentage of phases effectively present in the powders produced. The increase in the calcination temperature under an oxygen rich atmosphere induces a reduction in the surface area, in the volumes of pores and in the crystallite size, and increases the particle size as measured by BET. These characteristics of the electrocatalysts are strongly dependent on the phases present and their relative proportions. The increase in the amount of CeO_2 and on its crystalline character at the higher heat treatment temperatures result in a decrease of the crystallite size and of the specific area due to the fact that higher temperatures favor the crystallization of CeO_2 and because these smaller sized particles become supported by the still existing $CeAlO_3$ bigger sized particles, as depicted in Fig. 4.

Treating the oxidized sample under a reducing atmosphere causes an important reduction in the material's specific surface area and an increase in the particle size, making it possible to correlate these factors with the consumption of hydrogen during the treatment. Ce^{3+} cations most likely occupy octahedron sites in alumina, tending to be prevalent on its surface. At the same time, such an occupation of these sites by the Ce^{3+} cations may impede the transition of the Al^{3+} cations from tetrahedron to octahedron sites during the treatment, leading to a decrease in the surface area. The behavior shown by the present electrocatalyst samples regarding surface area, particle size, crystallite size and phases proportions are well compatible with the morphological results obtained by MET and SEM.

The density figures calculated for alumina (3.99 g/cm^3) and ceria (7.22 g/cm^3) were in direct agreement with those reported by PCPDF (10-0173) and (43-1002), respectively.

Upon heat treating the electrocatalytic powders at 1300 °C, it was possible to detect and quantify the crystalline Al_2O_3 present in the samples, as depicted in Table 6. The amounts of crystalline alumina found were compatible with the aluminum molar fraction contents found by utilizing the X-ray data to

Table 7
Rietveld based chemical composition determination.

Sample	Rietveld based chemical composition determination			
	Ce (%wt/wt)	Al (%wt/wt)	Ce (mol%)	Al (mol%)
CeAl3Tr13	84.56	15.44	51. 50	48.50
CeAl4Tr13	83.55	16.45	49.45	50.55
CeAl6Tr13	84.50	15.50	51.00	49.00
CeAl8Tr13	84.30	15.70	50.8	49.20

determine Rietveld based chemical compositions as shown in Table 7.

The X-ray diffraction data from the powder heat treated at 1300 °C, presented in Table 6 and analyzed by the Rietveld method, had its chemical composition and phase concentration determined. The chemical composition therein found and presented in Table 7 was closer to the nominal composition, 1:1 molar composition of Ce:Al, than that determined by the X-ray fluorescence. This result proves that there was amorphous alumina present in the samples treated at the lower heat treating temperatures.

Refining the data obtained for all electrocatalyst allowed the determination of the structural parameters for CeO_2 and Al_2O_3, as depicted in Table 8. Moreover, the lattice parameter for each sample heat treated at the higher temperature was obtained and is presented in Table 9.

The compositional and structural parameters presented in Tables 7–9 fully characterize the presence of amorphous alumina in the synthesized ceramic powders and explain the deviations from the expectable chemical compositions of cerium and aluminum determined by X-ray fluorescence, as depicted in Table 1. It is inferred that the structural condition of the aluminum oxide in the electrocatalyst developed strong influences in their phase transformation during calcination heat treatments. The amorphous alumina present in the synthesized powder is fully crystallized during the procedures for the SOFC anode preparation because of the elevated temperatures reached during the anode sintering procedures, in the order of 1500 °C. The powder herein prepared to be used as an electrocatalyst for multifunctional SOFC satisfied the basic requirements for this application. In order to analyze the feasibility of actually utilizing the proposed electrocatalyst to be processed into an SOFC anode material to work in conjunction with YSZ, the ceramic powder was calcined after fabrication at a temperature of 1200 °C, yielding an average particle size of 4.1 ± 0.9 μm and specific BET surface equal to 3.9 $m^2\,g^{-1}$. Furthermore, pre-pressed disc shaped specimens presented shrinkage of about 15.4% after firing at 1300 °C, indicating compatibility with YSZ [42]. In addition, successful electrochemical results from SOFC operation using the proposed ceramic material under direct ethanol or hydrogen feeding as fuels will be presented in a forthcoming article.

Table 8
Structural parameters for CeO_2 and Al_2O_3 in space group: FM-3M with $a = 0.54107$ nm and R-3C with $a = b = 0.47570$ nm $c = 1.29793$ nm, respectively.

Sample/atoms	Type	x	y	z	B_{iso}
CeAl3Tr13					
Ce	Ce^{4+}	0.0000	0.00000	0.00000	0.2900
	O^{2-}	0.25000	0.25000	0.25000	1.8200
Al	Al^{3+}	0.00000	0.00000	0.35215	0.3100
	O^{2-}	0.30966	0.00000	0.25000	0.3300
CeAl4Tr13					
Ce	Ce^{4+}	0.00000	0.00000	0.00000	0.2900
	O^{2-}	0.25000	0.25000	0.25000	1.8200
Al	Al^{3+}	0.00000	0.00000	0.34435	0.3100
	O^{2-}	0.32093	0.00000	0.25000	0.3300
CeAl6Tr13					
Ce	Ce^{4+}	0.00000	0.00000	0.00000	0.2900
	O^{2-}	0.25000	0.25000	0.25000	1.8200
Al_2	Al^{3+}	0.00000	0.00000	0.35181	0.3100
	O^{2-}	0.30824	0.00000	0.25000	0.3300
CeAl8Tr13					
Ce	Ce^{4+}	0.00000	0.00000	0.00000	0.2900
	O^{2-}	0.25000	0.25000	0.25000	1.8200
Al	Al^{3+}	0.00000	0.00000	0.35029	0.3100
	O^{2-}	0.30753	0.00000	0.25000	0.3300
CeAl9Tr13					
Ce	Ce^{4+}	0.00000	0.00000	0.00000	0.2900
	O^{2-}	0.25000	0.25000	0.25000	1.8200
Al	Al^{3+}	0.00000	0.00000	0.35134	0.3100
	O^{2-}	0.30565	0.00000	0.25000	0.3300

Table 9
Alumina and ceria lattice parameters for the indicated samples.

Phase	Al_2O_3		CeO_2
Sample type	Rhombohedral unit cell with space group R-3C		Cubic unit cell with space group FM-3m
	$a = b$(nm)	c (nm)	a(nm)
CeAl3Tr13	0.47570	1.29793	0.54107
CeAl4Tr13	0.47558	1.29526	0.54094
CeAl6Tr13	0.47560	1.29796	0.54107
CeAl8Tr13	0.47565	1.29828	0.54112
CeAl9Tr13	0.47552	1.29830	0.54107

5. Conclusions

$CeAlO_3/CeO_2$–Al_2O_3 nanosized-particle electrocatalyst powder was synthesized and fully characterized in terms of particle morphology and structural properties with the objective to prepare it to be applied in the fabrication of multifunctional SOFC anodes. It was demonstrated that cerium aluminate undergoes reversible oxidation–reduction reactions, being oxidized in air into cerium and aluminum oxides and reduced back under a hydrogen atmosphere into $CeAlO_3$. Depending on the oxidation temperature used to heat treat the synthesized powder, a fairly important amount of the aluminum oxide is in the amorphous state. This was observed for samples that underwent oxidation heat treatments in air conducted at 900 °C, a situation in which alumina was not detected by X-ray diffraction analysis. However, Raman spectroscopy spectra showed the presence of alumina in that sample type. Additionally, Al_2O_3 sharp X-ray peaks and Raman spectroscopy characteristic bands were clearly determined after a thorough crystallization procedure at 1300 °C for which about 22.0% (in mass) of alumina phase was found. The present all-ceramic potential SOFC anode material presents an interesting redox behavior. The reduced material is composed of $CeAlO_3$, which is fully transformed into ceria and alumina under an oxidizing atmosphere and fully reduced back into $CeAlO_3$ under a reducing atmosphere.

Acknowledgements

The authors would like to acknowledge the financial support of this research by CNPq (SAV's scholarship) and by the

business enterprise EnergiaH. The authors are also indebted to Ann Mari Svensson for reviewing the manuscript.

References

[1] P.E.V. Miranda, S.A. Venâncio, H.V. Miranda, Method for the direct oxidation and/or internal reforming of ethanol, solid oxide fuel cell for direct oxidation and/or internal reforming of ethanol, catalyst and multifunctional electrocatalytic anode for direct oxidation and/or internal reforming of ethanol, INPI process no. PI0901921-9, 17 June 2009.

[2] H.L. Tuller, A.S. Nowich, Doped ceria as a solid oxide electrolyte, Journal of the Electrochemical Society 122 (1975) 255–259.

[3] R.N. Blumenthal, F.S. Brugner, J.E. Garnier, The electrical conductivity of CaO-doped nonstoichiometric cerium dioxide from 700 to 1500 °C, Journal of the Electrochemical Society 120 (1973) 1230–1237.

[4] O. Costa-Nunes, R.M. Ferrizz, R.J. Gorte, J.M. Vohs, Structure and thermal stability of ceria films supported on YSZ (1 0 0) and α-Al_2O_3 (0 0 0 1), Surface Science 592 (2005) 8–17.

[5] J. Kaspar, P. Fornasiero, M. Graziani, Use of CeO_2-based oxides in the three-way catalysis, Catalysis Today 50 (1999) 285–298.

[6] A. Trovarelli, Catalytic properties of ceria and CeO_2-containing materials, Catalysis Reviews 38 (1996) 439–520.

[7] E.S. Putna, T. Bunluesin, X.L. Fan, R.J. Gorte, J.M. Vohs, R.E. Lakis, T. Egami, Catalysis Today 50 (1999) 343–352.

[8] A. Piras, A. Trovarelli, G. Dolcetti, Remarkable stabilization of transition alumina operated by ceria under reducing and redox conditions, Applied Catalysis B: Environmental 28 (2000) L77–L81.

[9] S. Damyanova, C.A. Perez, M. Schmal, J.M.C. Bueno, Characterization of ceria-coated alumina carrier, Applied Catalysis A: General 234 (2002) 271–282.

[10] J.Z. Shyu, W.H. Weber, H.S. Gandhi, Surface characterization of alumina-supported ceria, The Journal of Physical Chemistry 92 (1988) 4964–4970.

[11] N.P. Bradon, S. Skinner, B.C.H. Steele, Recent advances in materials for fuel cells, Annual Reviews Materials Research 33 (2003) 183–213.

[12] M. Mogensen, Ceria-based electrodes, in: A. Trovarelli (Ed.), Catalysis by Ceria and Related Materials, Catalysis Science Series, Imperial College Press, 2002, pp. 453–481 (Chapter 15).

[13] A. Atkinson, S. Barnett, R.J. Gorte, J.T.S. Irvine, A.J. McEvoy, M. Mogensen, S.C. Singhal, J. Vohs, Advanced anodes for high-temperature fuel cells, Nature Materials 3 (2004) 17–27.

[14] S. Park, J.M. Vohs, R.J. Gorte, Direct oxidation of hydrocarbons in a solid-oxide fuel cell, Nature 404 (2000) 265–267.

[15] R.J. Gorte, J.M. Vohs, Novel SOFC anodes for the direct electrochemical oxidation of hydrocarbons, Journal of Catalysis 216 (2003) 477–486.

[16] O.A. Marina, M. Mogensen, High-temperature conversion of methane on a composite gadolinia-doped ceria–gold electrode, Applied Catalysis A: General 189 (1999) 117–126.

[17] H.N. Kim, H.J. Park, G.M. Choi, The effect of alumina addition on the electrical conductivity of Gd-doped ceria, Journal Electroceramics 17 (2006) 793–798.

[18] A.S. Prakash, C. Shivakumara, M.S. Hegde, Single step preparation of CeO_2/$CeAlO_3$/γ-Al_2O_3 by solution combustion method: Phase evolution, thermal stability and surface modification, Materials Science and Engineering: B 139 (2007) 55–61.

[19] C.-T Chu, B. Dunn, Preparation of high-Tc superconducting oxides by the amorphous citrate process, Journal of American Ceramic Society 70 (1987) 375–377.

[20] D.R. Ricci, F. Ambrózio Filho, Caracterização de pós utilizando-se métodos de determinação de tamanho médio de partículas, Cerâmica 30 (1984) 337–346.

[21] A. Guiner, X-ray Diffraction: In Crystals, Imperfect Crystals, and Amorphous Bodies, Dover Publications Inc., New York, 1994.

[22] P. Courty, H. Ajot, C. Marcill, B. Delmon, Oxydes mixtes ou en solution solide sous forme très divisée obtenus par décomposition thermique de précurseurs amorphes, Powder Technology 7 (1973) 21–38.

[23] M. Kakihana, S. Kato, M. Yashima, M. Yoshimura, Preparation of tetragonal ZrO_2–12 mol% CeO_2 and ZrO_2–6 mol% $YO_{1.5}$ solid solutions at reduced temperature by a simple aqueous solution route using citric acid as a complexant, Journal of Alloys Compounds 280 (1998) 125–130.

[24] M.S.G. Baythoun, F.R. Sale, Production of strontium-substituted lanthanum manganite perovskite powder by the amorphous citrate process, Journal of Materials Science 17 (1982) 2757–2769.

[25] C.T. Chu, B. Dunn, Preparation of high-T_c superconducting oxides by the amorphous citrate process, Journal of the American Ceramic Society 70 (1987) C375–C377.

[26] S.T. Aruna, N.S. Kini, S. Shetty, K.S. Rajam, Synthesis of nanocrystalline $CeAlO_3$ by solution-combustion route, Materials Chemistry and Physics 119 (2010) 485–489.

[27] S.T. Aruna, N.S. Kini, K.S. Rajam, Solution combustion synthesis of CeO_2–$CeAlO_3$ nano-composites by mixture-of-fuels approach, Materials Research Bulletin 44 (2009) 728–733.

[28] S.A. Hassanzadeh-Tabrizi, E. Taheri-Nassaj, Synthesis of high surface area Al_2O_3–CeO_2 composite nanopowder via inverse co-precipitation method, Ceramics International 37 (2011) 1251–1257.

[29] A.K. Deb, P. Chatterjee, S.P. Sen Gupta, Synthesis and microstructural characterization of α-Al_2O_3–t-ZrO_2 composite powders prepared by combustion technique, Materials Science Engineering: A 459 (2007) 124–131.

[30] S. Biamino, P. Fino, M. Pavese, C. Badini, Alumina–zirconia–yttria nanocomposites prepared by solution combustion synthesis, Ceramics International 32 (2006) 509–513.

[31] W.H. Zachariasen, Crystal chemical studies of the 5f-series of elements XII. New compounds representing known structure types, Acta Crystallographica 2 (1949) 388–390.

[32] Y.S. Kim, Structural crystallography and crystal chemistry, Acta Crystallographica B 24 (1968) 295–296.

[33] M. Tanaka, T. Shishido, H. Horiuchi, N. Toyota, D. Shindo, T. Fukuda, Structure studies of $CeAlO_3$, Journal of Alloys and Compounds 192 (1993) 87–89.

[34] L. Vasylechko, A. Senyshyn, D. Trots, R. Niewa, W. Schnelle, M. Knapp, $CeAlO_3$ and $Ce_{1-x}R_xAlO_3$ (R: La, Nd) solid solutions: Crystal structure, thermal expansion and phase transitions, Journal of Solid State Chemistry 180 (2007) 1277–1290.

[35] W.T Fu, D.J.W. Ijdo, The structure of $CeAlO_3$ by Rietveld refinement of X-ray powder diffraction data, Journal Solid State Chemistry 177 (2004) 2973–2976.

[36] A. Feteira, D.C. Sinclair, M.T. Lanagan, Structural and electrical characterization of $CeAlO_3$ ceramics, Journal of Applied Physics 101 (2007), 064110-1-064110-7.

[37] S. Humbert, A. Colin, L. Monceaux, F. Oudet, P. Courtine, Simultaneous atmosphere and temperature cycling of three-way automotive exhaust catalysts, Studies in Surfarce Science Catalysis 96 (1995) 829–839.

[38] R.D. Shannon, Crystal physics, diffraction, theoretical and general crystallography, Acta Crystallographica A 32 (1976) 751–767.

[39] J.S Lee, K.H. Choi, B.K. Ryub, B.C. Shin, S.I.S. Kim, Effects of alumina additions on sintering behavior of gadolinia-doped ceria, Ceramics International 30 (2004) 807–812.

[40] S. Boullosa-Eiras, E. Vanhaecke, T. Zhao, D. Chen, A Holmen, Raman spectroscopy and X-ray diffraction study of the phase transformation of ZrO_2–Al_2O_3 and CeO_2–Al_2O_3 nanocomposites, Catalysis Today 166 (2011) 10–17.

[41] A. Martínez-Arias, M. Fernández-Garcıas, L.N. Salamanca, R.X. Valenzuela, J.C. Conesa, J. Soria, Structural and redox properties of ceria in alumina-supported ceria catalyst supports, The Journal of Physical Chemistry B 104 (2000) 4038–4046.

[42] Weitao Bao, Qibing Chang, Guangyao Meng, Effect of NiO/YSZ compositions on the co-sintering process of anode-supported fuel cell, Journal of Membrane Science 259 (2005) 103–109.